Acoustically driven degradation in single crystalline Si solar cell

O Ya Olikh

Faculty of Physics, Taras Shevchenko National University of Kyiv, Kyiv 01601, Ukraine

E-mail: `olikh@univ.kiev.ua`

Abstract. The experimental investigation of ultrasound influence on the silicon solar cell current-voltage characteristic has been carried out. The experiments were carried out by using longitudinal and transverse ultrasound waves in the temperature range from 290 to 340 K. The investigation has revealed the acoustically driven reversible increment of an ideality factor and decrement of a carrier lifetime both in the space charge region and in the solar cell base, a photocurrent, an open–circuit voltage, a fill factor, and a shunt resistance. The models of coupled defect level recombination, Shockley–Read–Hall recombination, and dislocation–induced impedance were used to describe the processes in the space charge region, in the solar cell base, and shunt resistance respectively. The role of oxide precipitates in an recombination and in an acousto–defect interaction has been discussed. It has been shown that the acoustically induced increase of carrier capture coefficient of point or extended defects is a reason of observed effects and qualitative model of ultrasound influence has been proposed.

Keywords: *silicon, solar cells, ultrasound influence*

1. Introduction

The silicon solar cells (SSC) are still dominant in the photovoltaic (PV) field due to their high efficiency, low selling price and process maturity. Therefore, understanding the way of material properties modification is a top priority for most of PV device manufacturers. It is known, for example, the loss in the SSC efficiency is observed in consequence of excess carrier injection by above-bandgap illumination or forward biasing [1, 2, 3, 4] (so–called light–induced degradation or LID), high voltage stress [5, 6, 7] (potential–induced degradation or PID), or radiation treatment [8, 9] (irradiation–induced degradation or IID). Degradation reasons are processes in crystal defect sub-system under external influence. It is may be a transformation of the boron-oxygen or copper-contained complex (for the LID case), a decoration of stacking faults by sodium (PID case) or a creation of radiation–induced recombination centers (IID case). The partial or full SSC efficiency recovery is observed quite often during of subsequent annealing at an elevated temperature.

On the other hand, it has been shown experimentally that ultrasonic waves (USWs) can be the effective instrument for defect engineering in silicon. In particular, ultrasound is used to affect a carrier diffusion length [10, 11], to vary a current in p–n structures and Schottky diodes [12, 13, 14, 15, 16, 17], to transform an impurity defect [18, 19, 20, 21], to change a spectrum [22] and density [23] of surface states. Frequently the crystal and device properties recover after stopping of ultrasound action at room temperature even [10, 11, 12, 18].

This article presents the result of experimentally investigation of the acoustic strain field influence on the electrical characteristic of the n$^+$–p SSC. Ultrasound has been found to result the decrease of carriers lifetime and, accordingly, solar cell efficiency. The USWs intensity did not exceed 0.5 W/cm^2 and the full recovery of cell characteristics was observed after the stop of an acoustic wave propagation. Dependencies of such sound induced degradation on USW type and intensity are presented. The findings are discussed by using models of coupled defect level recombination, Shockley–Read–Hall (SRH) recombination, and dislocation–induced impedance.

2. Experimental and calculation details

The investigated solar cell was created on 2 inch p-type CZ-Si:B wafers with doping level of 1.4×10^{15} cm^{-3} and thickness of 300 μm. The n$^+$ emitter with carrier concentration of about 10^{19} cm^{-3} and thickness of 0.5 μm was formed by phosphorus implantation. Then wafer surface was passivated by Al$_2$O$_3$ film and further capped by TiO$_x$ as antireflective coating. Finally the aluminium front (metal grid) and rear (solid contact) electrodes were deposited by screen printing before rapid annealing. The samples with area of 1.5 to 2.1 cm^2 used in our experiments were cut from the central part of the wafer.

The dark and illuminated forward current-voltage (I–V) characteristics of the samples both with and without ultrasound loading (USL) were measured over a temperature range 290–340 K. The sample temperature was controlled by differential copper-constantan thermocouple. Some curves are shown in Figure 1.

The classical double-diode model of n$^+$–p SSC I–V characteristics expressed in the following form:

$$I(V,T) = -AJ_{ph} + \frac{qAn_i d}{2\tau_g} \left\{ \exp\left[\frac{q(V - IR_s)}{nkT}\right] - 1 \right\}$$
$$+ \frac{qAn_i^2}{p_p}\sqrt{\frac{\mu_n kT}{\tau_n}} \left\{ \exp\left[\frac{q(V - IR_s)}{kT}\right] - 1 \right\} + \frac{V - IR_s}{R_{sh}}, \qquad (1)$$

where A is the cell area, J_{ph} is the photocurrent density, n_i is the intrinsic carrier concentration, τ_g is the carrier lifetime in the space charge region (SCR), d is the SCR thickness:

$$d(V,T) = \sqrt{\frac{2\varepsilon\varepsilon_0(p_p + n_n)}{qp_p n_n}\left[\frac{E_g}{q} - \frac{kT}{q}\ln\left(\frac{N_v N_c}{p_p n_n}\right) - \frac{2kT}{q} - V\right]}, \qquad (2)$$
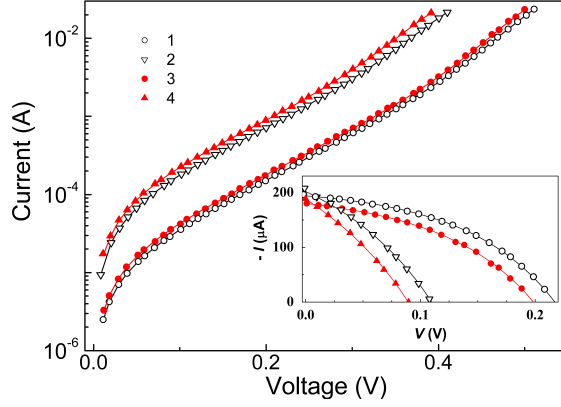
Figure 1. SSC dark I–V characteristics measured at 301 K (curves 1, 3) and 341 K (curves 2, 4) with (2, 4) and without(1, 3) USL. $W_{US} = 0.40$ W/cm^2. Inset: Parts of illuminated I–V characteristics in the voltage range from 0 to V_{oc}. The lines are the fitted curves using Eq. (1).

ε is the permittivity (11.7 for Si), p_p and n_n are the majority carrier concentration in the p– and n–type regions, E_g is the semiconductor band gap, N_c and N_v are the effective density of states in the conduction and valence bands; n is the ideality factor of the nonideal current components, R_s and R_{sh} are the series and shunt resistances of the device, μ_n and τ_n are the electron (minority carrier) mobility and lifetime outside SCR in the diode base. The current-voltage equation that models the solar cell by an equivalent electrical circuit contains several parameters related to physical phenomena occurring in the device. It is commonly believed that $I_{01} = (qAn_i^2/n_n)\sqrt{\mu_n kT/\tau_n}$ is closely related to recombination in the quasi-neutral region, while $I_{0n} = (qAdn_i/2\tau_g)$ reflects the overall recombination in the SCR.

We used Eqs. (1) and (2) to fit the experimental data and the I_{ph} (for illuminated I–V curves only), τ_g, τ_n, n, R_{sh}, and R_s were taken as the fittings parameters. It was supposed that $n_i = 1.64 \times 10^{15} T^{1.706} \exp(-E_g/2kT)$ [24] and temperature dependencies of E_g and μ_n followed Varshni and Caughey–Thomas equations [25, 26]

$$E_g(T) = 1.169 - 7.021 \cdot 10^{-4}T^2/(T + 1108)\,, \tag{3}$$

$$\mu_n(T) = \mu_{min} + \frac{\mu_0}{1 + (p_p/N_{ref})^\zeta}\,. \tag{4}$$

The temperature dependence of the μ_{min}, μ_0, N_{ref} and ζ has the form $P = P_0(T/300)^\gamma$ and parameters value are given in the [25], Table A8.2. The fitting were done by using the differential evolution method [27] and extremely good fit to the experimental data was obtained — see Figure 1.

The monochromatic light was used for SSC illumination. The light wavelength of $\lambda = 900$ nm ensured the electron-hole pair generation in the p-region mainly and low light intensity of $W_{ph} = (8 \pm 4)$ W/m^2 was chosen to avoid any LID processes. The short–circuit current density J_{sc}, open–circuit voltage V_{oc} and the fill factor FF were estimated from illuminated I–V curves by the conventional mode. It should be

noted that $J_{sc} \approx J_{ph}R_{sh}/(R_{sh} + R_s)$. In the case of the samples under investigation, R_s was defined by contact resistance and was about 1 Ω, R_{sh} overrode 2 kΩ. Therefore it is expected that $J_{sc} \approx J_{ph}$. Really such relation was observed for the J_{ph}, which was obtained by whole I–V curve fitting, and J_{sc}, which was obtained as a point of intersection of a I–V curve with a current axis.

In the USL case, the acoustic waves were exited with help of a piezoelectric transducer and were injected in the samples from the base side in the [111]-direction. The longitudinal (L–USL) and transverse (T–USL) waves were used. The ultrasound frequency f_{US} and intensity W_{US} were 8.0 MHz and 0.18 W/cm^2 (in the L–USL case) and 4.2 MHz and up to 0.4 W/cm^2 (in the T–USL case). It was reported previously [19, 17, 11] that a characteristic time of change in the silicon structure parameters under the ultrasound action did not exceed $2 \cdot 10^3$ s. In order to wait till the acoustically induced (AI) transitional period the following experimental procedure has been used. After USL start the sample was kept at room temperature during 60 min and then the I–V measurements and the sample heating were started. In order to avoid the effect of piezoelectric field on I–V characteristics, the piezoelectric cell has been shielded.

The samples from the investigated set differed in the shunt resistance mainly. In the article the typical results for the samples with low (approximately 10^4 Ω at room temperature) and high ($> 10^{15}$ Ω) R_{sh} value are presented. The samples were labeled as SC–R4 and SC–R15 respectively.

3. Results and Discussion

3.1. Ultrasound influence on the SCR recombination

Figure 2(a) and Figure 2(b) show the USL influence on SCR carrier lifetime and ideality factor respectively. One can see that USL leads to τ_g decrease and n increase. The relative change of SCR carrier lifetime $\varepsilon_{\tau g}$ and absolute change of ideality factor Δn do not depend practically on the temperature over the investigated range and are presented in Table 1. The extent of AI effect is weakly depend on both ultrasound intensity and wave type and becomes more apparent in the SC–R15 sample. The L–USL and T–USL differed by f_{US} too, but it was shown previously [13, 28], that ultrasound influence on the silicon structures had arose with wave frequency. f_{US} of the L–USL is greater than in the case of transverse wave using, but T–USL is more effective (see Figure 2, Table 1). Therefore the crucial factor of the ultrasound influence on the SSC parameters is the wave type.

Initially, we want to stress, that reversibility of the acoustically driven effects testifies that ultrasound doesn't make change in defect concentration as well as doesn't cause defect diffusion. Before the causes of ultrasound influence would be discussed, the recombination mechanism must be identified. Firstly the large ideality factor and small carrier lifetime (about 10^{-8} s at room temperature) must be accentuated. An ideality factor larger than 2 cannot be explained by classical SRH-theory. Several attempts to
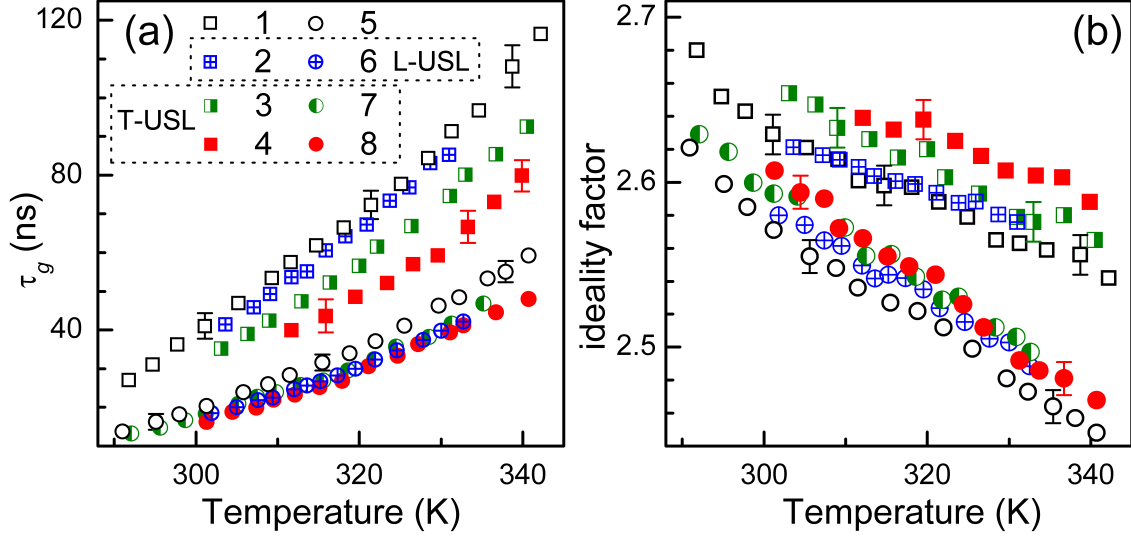
Figure 2. Temperature dependences of SCR carrier lifetime (a) and ideality factor (b) for the SC–R15 (squares, curves 1–4) and SC–R4 (circles, curves 5–8) with (curves 2–4 and 6–8) and without (1 and 5) USL. The longitudinal (2, 6) and transverse (3, 4, 7, 8) ultrasound waves were used. W_{US},W/cm^2: 0.18 (2, 6), 0.19 (3), 0.22 (7), 0.40 (4, 8).

Table 1. USL parameters and acoustically induced changes of SSC parameters.

Sample	SC–R4			SC–R15		
Wave type	L	T	T	L	T	T
W_{US} (W/cm^2)	0.18	0.22	0.40	0.18	0.19	0.40
ξ_{US} (10^{-6})	1.3	3.1	4.2	1.3	2.8	4.2
u_{US} (nm)	0.3	0.7	0.9	0.3	0.6	0.9
Δn (10^{-3})	16 ± 10	24 ± 10	28 ± 10	10 ± 10	22 ± 10	43 ± 10
$-\varepsilon_{\tau g}$ (%)	12 ± 5	14 ± 5	17 ± 5	5 ± 5	18 ± 5	30 ± 5
$-\varepsilon_{\tau n}$ (%)	11 ± 12	43 ± 12	58 ± 12	13 ± 12	71 ± 12	85 ± 12
$-\varepsilon_{\tau n}^{Jph}$ (%)	2 ± 15		39 ± 15	14 ± 15		54 ± 15
K_{US} (10^6 W/cm^{2}s)	0.2 ± 0.1	1.0 ± 0.2		0.3 ± 0.1	6.5 ± 0.5	
$-\varepsilon_{Rdis}$ (%)	–	–	–	0	23 ± 15	40 ± 15
$-\varepsilon_{Jph}$ (%)	0 ± 1		9 ± 1	0 ± 1		4 ± 1
$-\varepsilon_{Voc}$ (%)	3 ± 2	4 ± 2	13 ± 2	2 ± 2	6 ± 2	11 ± 2
$-\varepsilon_{FF}$ (%)	2 ± 2	2 ± 2	5 ± 2	2 ± 2	3 ± 2	4 ± 2

explain large n have been made with various models. For example, according to van der Heide *et al.*[29], a nonuniform contact resistance of the front side metallisation leads to a high n value. However, this theory predicts the dependence of ideality factor on light intensity, whereas change of n value with W_{ph} variation is not observed in our case. Beier and Voss [30] explained the large n by saturation effects within the SRH-model for several donor-like levels. However, this theory is unable to explain the magnitude of the recombination current I_{0n}, which is orders of magnitude larger than expected for silicon. The high ideality factor was attributed to deep-level-assisted tunneling [31, 32] too. But according to this model, the ideality factor is fairly constant versus temperature, whereas such dependencies are observed experimentally — see Figure 2(b).

At the same time, the experimentally observed large n and small τ_g can be explained by the model of coupled defect level recombination [33, 34]. This model provides a rapid direct charge transfer between defect levels. Initially [33], it was suggested, that at least one shallow level participated. Subsequently the model of the donor-acceptor-pair (DAP) recombination (via deep levels) was proposed [34].

According to the DAP recombination model both n and τ_g depend on the hole and electron capture cross sections (σ_p and σ_n) as well as on coupling parameter r_{DA}. By-turn, $\sigma_{n,p}$ and r_{DA} depend on the distance between donor and acceptor r and in the simplified case can be expressed as [34]:

$$\sigma_{n,p}(r) = \sigma_{n,p}^0 \left(\frac{r}{C_r} \right)^2 , \tag{5}$$

$$r_{DA}(r) = c_{DA}^0 N_D N_A \left[1 + \frac{r}{a_0} + \frac{1}{3} \left(\frac{r}{a_0} \right)^2 \right] \exp \left(-\frac{r}{a_0} \right) , \tag{6}$$

where σ_n^0 and σ_p^0 are capture the cross sections of the isolated donor and acceptor, N_D and N_A are the donor and acceptor concentration, a_0 is the defect Bohr radius, C_r and c_{DA}^0 are some constant. In particular [33], if no carrier exchange between the donor level and the valence band as well as between the acceptor level and the conduction band are assumed then the total recombination rate will be

$$R = R_{12} - \sqrt{R_{12}^2 - \frac{np - n_i^2}{\tau_{D,n}\tau_{A,p}(1-\epsilon)}} \tag{7}$$

with

$$R_{12} = \frac{(n + n_D)(p + p_A)}{2r_{DA}\tau_{D,n}\tau_{A,p}(1-\epsilon)} + \frac{\tau_{D,n}(p + p_D) + \tau_{A,p}(n + n_A)}{2\tau_{D,n}\tau_{A,p}(1-\epsilon)} . \tag{8}$$

$\tau_{D,n} \sim 1/\sigma_n^{0,D}$ and $\tau_{A,p} \sim 1/\sigma_p^{0,A}$ are the electron and hole lifetimes for the non-coupled donor and acceptor respectively, n_D, p_D, n_A, p_A and ϵ depend on the energy positions and degeneracy factors of the defect levels [33]. It is known, that $\tau_g \sim R^{-1}$. Unfortunately, the functional relation between ideality factor and DAP recombination parameters doesn't suggested, but n is shown [33, 35] to increase with the r_{DA} and lifetime decrement.

DAP model permits to explain the observed temperature dependencies of both n and τ_g – see Figure 2(a) and Figure 2(b). Actually, the capture cross section of
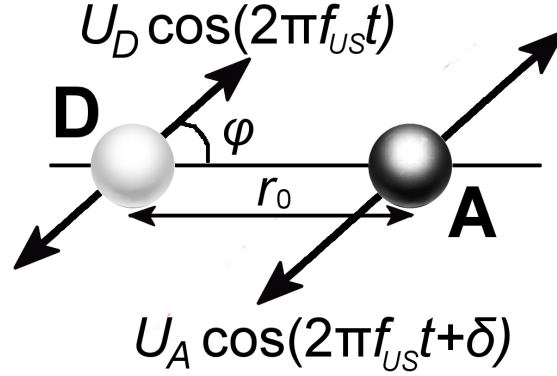
Figure 3. Behavior of DAP recombination center under USL condition.

the attractive centers is known [36, 37] to depend on temperature as T^{-1} up to T^{-3}. Therefore $\sigma_n^{0,D}$ and $\sigma_p^{0,A}$ reduce due to the temperature increase and cause the observed changes of the ideality factor and carrier lifetime. In addition, the difference in initial τ_g and n values for SC–R15 and SC–R4 (Figure 2,(a),(b) curves 1 and 5) can deal with large distance between coupled defects.

On our opinion, the reversible ultrasound influence deals with the alteration of the distance between donor and acceptor. Really, according to [38, 39], the force acting on the point defect during USL can be expressed as

$$F_d = K \, \Delta\Omega_d \frac{\partial \xi(x,t)}{\partial x} \, , \tag{9}$$

where K is the bulk elasticity modulus, $\Delta\Omega_d$ is volume elastic strain caused by the relaxation of the defect volume (e.g. $\Delta\Omega_d < 0$ and $\Delta\Omega_d > 0$ for vacancies and interstitial atoms, respectively), ξ is the crystal lattice deformation, and acoustic wave propagates along x direction. $\partial \xi(x,t)/\partial x$ linearly depends on the deformation amplitude $\xi_{US} = \sqrt{2W_{US}/\rho_{Si}\,\vartheta_{US}^3}$ (where $\rho_{Si} = 2.33$ g/m^3 is the silicon density, ϑ_{US} is the ultrasound velocity, equals to 9850 m/s and 5840 m/s for longitudinal and transverse wave respectively). Therefore, a point defect vibrates under USL condition and oscillation amplitude and phase are determined by both defect character and acoustic wave intensity and type.

Some qualitative conclusion can be drawn from the simplest model, which is shown on Figure 3. Initially two point defect, donor (D) and acceptor (A) are situated at distance r_0. During USL defects would vibrate with amplitudes u_D and u_A. The amplitudes depend on ξ_{US}, defect elastic strain ($\Delta\Omega_D$ and $\Delta\Omega_A$), defect coupling and can be different. δ is the phase shift between donor and acceptor vibration. If no ultrasound energy absorption by defect is assumed, then δ will equal to 0° and 180° in the case of $\Delta\Omega_D \cdot \Delta\Omega_A > 0$ and $\Delta\Omega_D \cdot \Delta\Omega_A < 0$ respectively. φ is the angle between the defect pair axis and the forced displacement direction.

Generally, the distance r between donor and acceptor would not equal to r_0 during vibration. Figure 4 and Figure 5 show relative changes of capture cross section
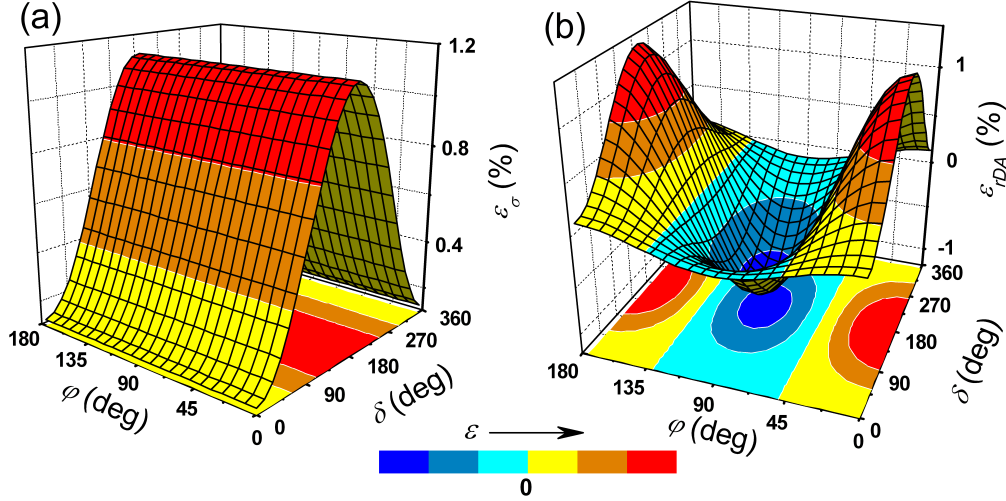
Figure 4. Simulated dependencies of AI changes of capture cross section (a) and coupling parameter (b) on the vibration phase shift and on the angle between the pair axis and the displacement direction. The parameters are set to $a_0 = 3.23$ nm, $r_0 = 10$ nm, $u_A = 1$ nm, $u_D = 0.5$ nm.
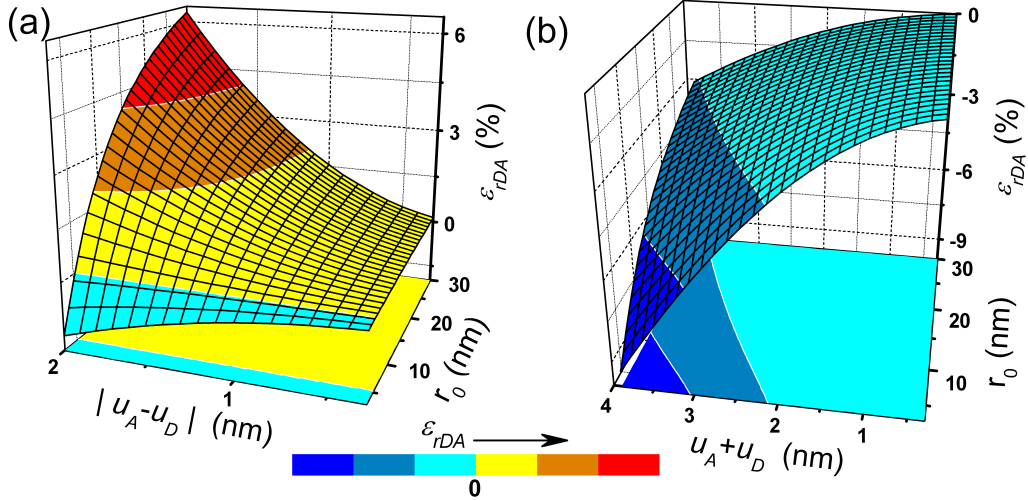

Figure 5. Simulated dependencies of AI changes of coupling parameter on the vibration amplitudes and on initial distance between donor and acceptor. The parameters are set to $\varphi = 0°$, $\delta = 0°$ (a) and $\varphi = 90°$, $\delta = 180°$ (b).

$\varepsilon_\sigma = [\sigma(r) - \sigma(r_0)]/\sigma(r_0)$ and coupling parameter $\varepsilon_{r_{DA}} = [r_{DA}(r) - r_{DA}(r_0)]/r_{DA}(r_0)$. ε_σ and $\varepsilon_{r_{AD}}$ are averaged over the ultrasound wave period. Under simulation (i) it was assumed, that relaxation time in the recombination sub-system was considerably less than f_{US}^{-1}; (ii) Eqs. (5) and (6) were used; (iii) the value $a_0 = 3.23$ nm from the [34] was utilized; (iv) the chosen u_D and u_A values were commensurate with the atom displacement u_{US} in acoustic wave (see Table 1). Simulations show that the extent of ultrasound influence on both r_{DA} and σ increases with r_0 decrease. In simple cases
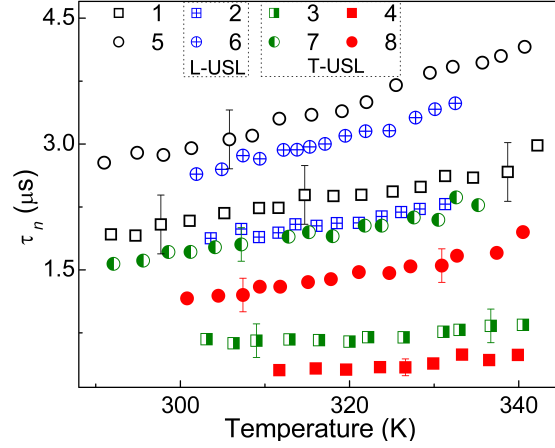
Figure 6. Temperature dependencies of base carrier lifetime for the SC–R15 (squares, 1–4) and SC–R4 (circles, 5–8) with (2–4 and 6–8) and without (1 and 5) USL. W_{US},W/cm^2: 0.18 (2, 6), 0.19 (3), 0.22 (7), 0.40 (4, 8).

$\delta = 0°$ or $\delta = 180°$, the amplitude dependencies of ε_σ and $\varepsilon_{r_{DA}}$ are determined by $|u_D - u_A|$ and $(u_D + u_A)$ respectively. In particular

$$\varepsilon_\sigma = \frac{(u_D \pm u_A)^2}{2r_0^2}. \tag{10}$$

Figure 4(a) and Eq. (10) show that the capture cross section increases under USL condition. AI alteration of coupling parameter is more complicated and sign of $\varepsilon_{r_{DA}}$ depends on φ and r_0 - see Figure 4(b) and Figure 5. But in the case of low r_0/a_0 value, DAP recombination is expected [33, 34] to be effective and the AI r_{DA} reduction is forecasted by Figure 5 even through $\varphi = 0°$.

According to the DAP recombination theory, σ increase and r_{DA} decrease must cause a lifetime reduction and an ideality factor rise. Just so effects are observed under USL condition. Under equal W_{US} value conditions T–USL is more effective due to the larger ε_{US} value (see Table 1). As mentioned above, the r_0 is probably smaller in SC–R15 than in SC–R4. On our opinion, it is a reason of the more remarkable AI effect in SC–R15.

3.2. Ultrasound influence on recombination in the SSC base

Temperature dependencies of the minority carrier lifetime in the p–region of SSC are shown in Figure 6. The SRH lifetime due a defect in p–type material at low injection level can be written as

$$\tau_n = (N_d \sigma_n \nu_{th})^{-1}, \tag{11}$$

where N_d is the concentration of the defect, ν_{th} is the thermal velocity. To our mind, the slight increment of τ_n with T results from the σ_n temperature dependency, which is mentioned above. As one can see, the USL causes the lifetime τ_n decrease, that runs
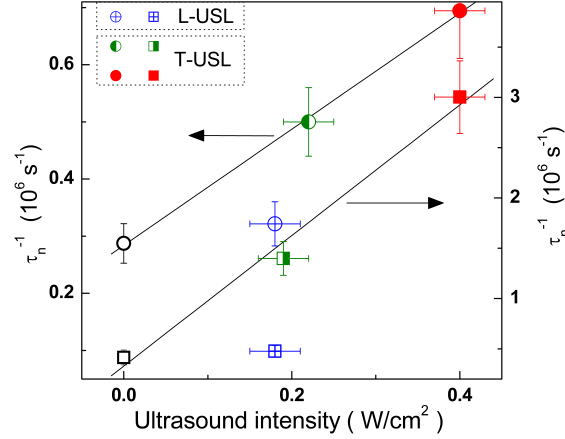
Figure 7. Dependencies of reciprocal lifetime in the SSC base on ultrasound intensity for the SC–R4 (circles, left axis) and SC–R15 (squares, right axis) at 320 K. Symbol filling is defined by the intensity and type of ultrasound waves and coincides with Figure 6 notation. Lines are linear fitting of T–USL data.

down to 20% of τ_n initial value. The relative AI change of an electron lifetime $\varepsilon_{\tau n}$ is presented in Table 1.

Ordinary the lifetime reduction under radiation action is described by the Messenger-Spratt equation [26]:

$$\tau_n^{-1} = \tau_{n0}^{-1} + K\Phi\,, \tag{12}$$

where τ_{n0} is the minority carrier lifetime in the unirradiated cell, Φ is the integrated flux, and K is a lifetime damage constant characteristic for the material and the type of irradiation. The dependencies of reciprocal lifetime on ultrasound intensity are shown on Figure 7. As one can recognize, the linear dependence of $1/\tau_n$ on W_{US} is observed. Therefore the modified Messenger-Spratt equation can be used to describe the acoustically driven change of the lifetime:

$$\tau_n^{-1} = \tau_{n0}^{-1} + K_{US}W_{US}\,, \tag{13}$$

where τ_{n0} is the lifetime in the ultrasound-free cell and K_{US} depends on a wave type and a sample state. The defined K_{US} values are listed in Table 1. Taking into account Eq. (11) and reversibility of ultrasound influence, we assume the observed decrement in lifetime to be evident of AI change of σ_n. In this case the following relation can be obtained by using Eqs. (11) and (13):

$$\frac{\varepsilon_\sigma}{\tau_{n0}W_{US}} = K_{US}\,. \tag{14}$$

The most recombination centers in the silicon are known to be a complex defect, which is composed of non-equivalent components. For example, the complexes of two point defects with an opposite charge occur quite often. Following the empirical relation proposed in [40], we believe, that the capture cross section of such pair depends on distance between complex's component and Eq. (7) is true. Hence the introduced in

Sec. 3.1 model of AI increase of σ is applicable to account for τ_n decrease. Really, according to the model $\varepsilon_\sigma \sim u_{D,A}^2 \sim \xi_{US}^2 \sim W_{US}$, i.e. the linear τ_n^{-1}–W_{US} relation is expected and is observed — see Figure 7. The K_{US} increment in the T–USL and SC–R15 cases (Table 1) relates to the larger ξ_{US}–W_{US} proportionality coefficient and smaller τ_{n0} value respectively. It should be noted that an initial distance between components of recombination center is much smaller than the distance between participants of DAP recombination; therefore according to Eq. (10), the more effective ultrasound influence is expected.

3.3. Light and annealing influence on the SSC parameters

Any concrete defect title was not referred as an recombination center in the discussion above. The additional investigations are necessary to define the type of defects, which are involved in both the recombination and the acousto–defect interaction.

It is known that the most harmful recombination centers in boron–doped Czochralski–grown SSC are the boron–oxygen related defects [41, 42, 1, 3], iron–boron pairs [41, 43, 44] (or another Fe–related trap in the n^+p–junctions [45, 46]), and oxide precipitates [47, 48, 41, 49, 50]. The first two defects are sensitive to an intensive illumination at room temperature. Thus transformation of boron–oxygen defects by an illumination leads to minority–carrier lifetime degradation (down to as 5 times as small [3]). Full lifetime recovery is observed after annealing at 200 °C for 10 min in the dark. The degradation–recovery cycle can be reiterated [42]. On the other hand, at room temperature, the vast majority of iron exists in iron–boron pairs, which can be readily dissociated under intense illumination to release interstitial iron. This gives a lifetime change which depends on doping concentration and excess carrier concentration [44]. After the dissociation procedure, the concentration of Fe_i decreases according to [41]

$$N_{Fe}(t) = (N_{Fe,0} - N_{Fe,eq}) \exp\left[-1.3 \cdot 10^{-3} p_p^{2/3} \exp\left(-\frac{0.68}{kT}\right) t\right] + N_{Fe,eq}, \quad (15)$$

where $N_{Fe,0}$ and $N_{Fe,eq}$ are the concentration after dissociation immediately and equilibrium concentration which remains a long time after dissociation respectively.

To inspect an availability of boron–oxygen defects and iron–boron pairs the following experimental procedure has been used. The samples were light soaked under halogen lamp (2 Suns) illumination at approximately 305 K. The illumination time varied from 1 h to 8 h. After illumination samples are stored in the dark at room temperature. To determine the kinetics of SSC parameters the dark I–V characteristics have been measured with interval 10–15 min at room temperature over a period 5 h after illumination stopping. To determine the permanent LID of SSC parameters the dark I–V characteristics have been measured in 48 h after illumination. After accumulated time under illumination had reached 10–15 h the samples were annealed at 200 °C for 10 min in the dark and SSC parameters were determined at room temperature. After that, the illumination–annealing cycle was repeated.

The results of residual influence of both illumination and annealing on an equilibrium value of SSC parameters are presented on Figure 8. In contrast to other
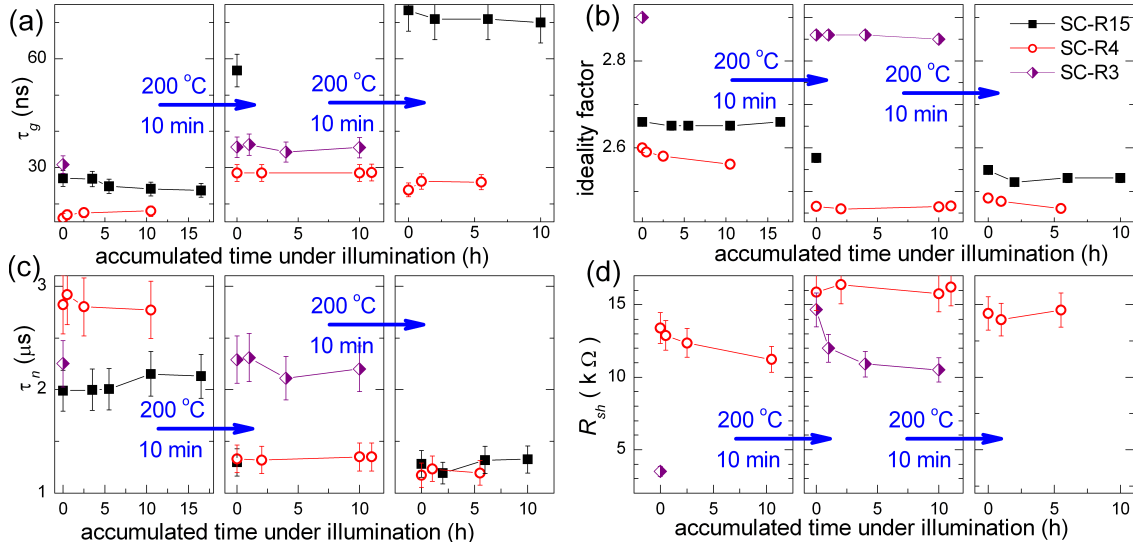
Figure 8. Dependencies of SCR carrier lifetime (a), ideality factor (b), base carrier lifetime (c), and shunt resistance (d) on accumulated illumination time and annealing. Data were obtained from I–V curves which had measured in 48 h after illumination or annealing at $T = 295$ K. Lines only serve as guide to the eye.

Figures, this contains sample SC–R3 data. The SC–R3 distinctive features are a low R_{sh} value and a performance of annealing before illumination. Though the obtained results for SC–R3 are similar to other samples. One can see that the illumination does not affect a SCR carrier lifetime as well as a base carrier lifetime neither before annealing, nor after. Illumination induced decrease of ideality factor is commensurable with an accuracy of n determination. Change of shunt resistance under illumination is most considerable but it reaches -20 % only and does not recur after an annealing – see Figure 8(d), curve for the sample SC–R4. Annealing had more efficient influence on SSC parameters and results in an increment of τ_g and R_{sh} as well as in a decrement of τ_n and n. Such behavior of SSC parameters under illumination and annealing action is evident of absence of boron–oxygen defects influence. The reason of light induced and annealing induced changes will not be further discussed since this is beyond scope of our study.

The typical dependencies of SSC parameters versus time since illumination stoping are shown on Figure 9. As one can see, τ_n and R_{sh} do not vary practically. Hence these parameters can not be influenced by iron–boron pairs. At the same time τ_g and n are changing after illumination. We supposed that the expressions, that have described the both τ_g and n evolution, were similar to Eq. (15) and used the characteristic time $\left[1.3 \cdot 10^{-3} (1.4 \times 10^{15})^{2/3} \exp\left(-\frac{0.68}{295k}\right)\right]^{-1} = 2.53 \cdot 10^4$ s to plot fitting line on Figure 9(a) and (b). The fitting is in good agreement with experimental data. Therefore pairs Fe_iB_s can affect a SCR recombination and the acceptor level $E_C - 0.23$ eV can be involved in a DAP recombination process. Incidentally, pair Fe_iB_s is a good candidate for acousto-active defect: the B is substitutional atom whose volume is smaller than the volume of
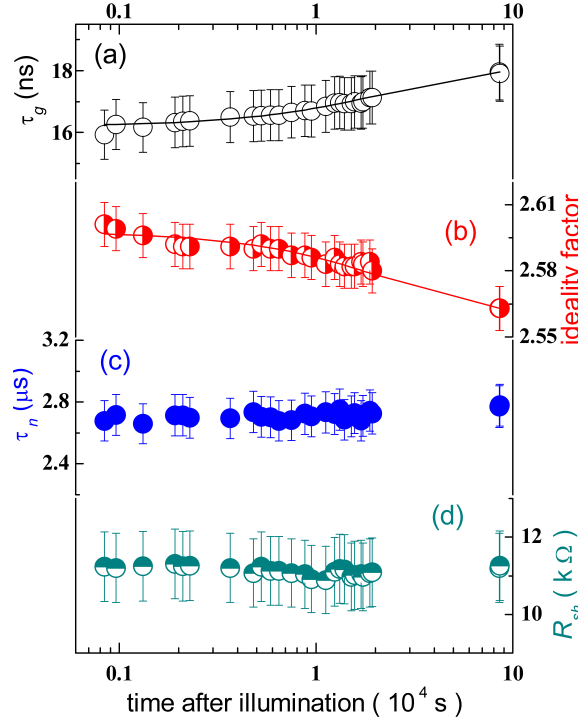
Figure 9. SCR carrier lifetime (a), ideality factor (b), base carrier lifetime (c), and shunt resistance (d) as a function of time since illumination stoping. Sample SC–R4. $T = 295$ K. Lines are plotted by using Eq. (15) and characteristic time $2.53 \cdot 10^4$ s.

the matrix atom and $\Delta\Omega_d(B_s) < 0$ whereas the interstitial Fe leads to $\Delta\Omega_d(Fe_i) > 0$. On the other hand, the τ_g change after illumination is about 10 % (see Figure 9(a)), whereas a capture cross sections change, which is expected due to pair dissociation, equals to 1.7 times for electrons and 0.04 times for holes [44]. Hence, on our opinion, the pair Fe_iB_s is not main reason of a SCR recombination in the investigated samples.

According to Murphy *et al.*[47, 49], the recombination at oxide precipitates cannot be explained by a single two–level defect alone and at least two independent defects are exist. These defects have single energy levels at $E_V + 0.22$ eV and $E_C − 0.08$ eV and have $\sigma_n/\sigma_p = 157$ and $\sigma_p/\sigma_n = 1200$ respectively [49]. So, these defects are suitable for the DAP recombination process. Dislocations and stacking faults surround the oxide precipitates and lead to capture coefficient change as well as to increase the concentrations of two defects, without introducing additional states into the bandgap [47, 41, 49] and can provide their acousto–activity. The oxide precipitates are nonuniformly distributed across a Cz–Si wafer [48] or a solar cell [50] and it is the probable reason for a SSC parameters variation from one investigated sample to another. On the basis of mentioned above, we conclude that the defects, involved in both recombination and acousto–defect interaction are oxide precipitates mainly.
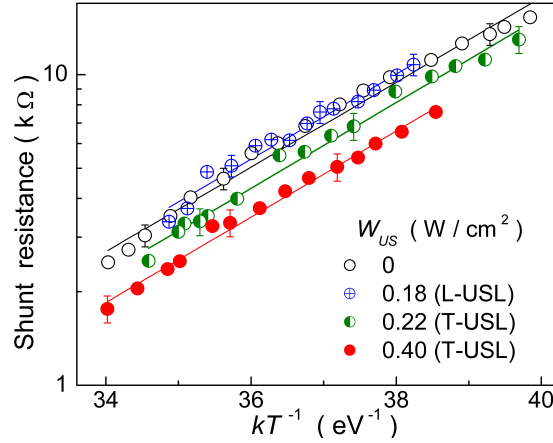
Figure 10. Plot of R_{sh} as the function of kT for the SC–R4 with and without USL. Lines are the fitted curves using Eq. (16)

3.4. Ultrasound influence on shunt resistance

Figure 10 illustrates R_{sh} modification for the sample under USL condition. One can see that the T–USL leads to moderate R_{sh} decrease whereas the L–USL does not change shunt resistance practically.

Several non-mechanical reasons of SSC shunt resistance appearance are known [51]. They are aluminum particles, macroscopic Si_3N_4 inclusions, inversion layers at precipitates. During firing Al will alloy in, leading to a p^+–doped region around the particle, which may compensate the emitter and may be in ohmic contact with the base. Subsequent annealing had to increase this p^+–region and to decrease R_{sh}. Such behavior conflicts with data, which are presented on Sec. 3.3. Inversion layers and Si_3N_4 inclusions occur in multicrystalline silicon cells mainly [51] and cannot cause a shunt resistance of the investigated samples too. On the other hand, dislocations, which intersect the junction, are generally held responsible as a possible source of ohmic current [51, 52, 53]. Dislocations should be strongly recombinative, its recombination current may become strong enough for it to act as a shunt. For this reason they should be decorated by impurities [51].

Gopal and Gupta [54, 55] introduced the model of dislocation–induced impedance of photovoltaic detector. According to this model, the R_{sh} can be given by

$$R_{sh} = kT R_{dis} \cosh\left(\frac{E_{dis} - E_i + U_s}{2kT}\right) \cosh\left(\frac{E_{dis} - E_i - U_s}{2kT}\right), \qquad (16)$$

with

$$R_{dis}^{-1} = \rho_{dis} A q^2 A_{dis} \sqrt{K_n K_p} N_{dis}(n_p + p_p), \qquad (17)$$

where E_{dis} is the energy level which significantly contributes to the dislocation recombination current, E_i is the intrinsic Fermi level, U_s is the potential at the surface of the dislocation core, ρ_{dis} and A_{dis} are the dislocation density and surface area, respectively, K_n and K_p are the capture probabilities for electrons and holes by the
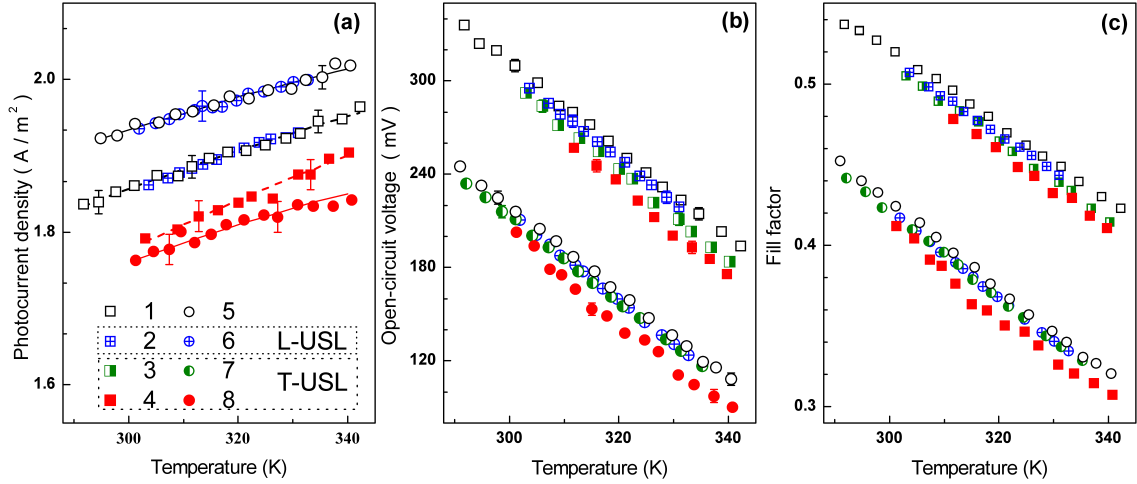
Figure 11. Temperature dependencies of photocurrent density (a), open–circuit voltage (b) and fill factor (c) for the SC–R15 (squares) and SC–R4 (circles) with (2–4 and 6–8) and without (1 and 5) USL. W_{US},W/cm^2: 0.18 (2, 6), 0.19 (3), 0.22 (7), 0.40 (4, 8). Lines are the fitted curves using Eq. (18).

dislocation states, N_{dis} is the density of surface states at each dislocation. Eq. (16) is reduced for the simplified case $K_p = K_n$. It should be noted that a similar temperature dependence of a SSC shunt resistance is used elsewhere [56] too.

We use Eq. (16) to fit the experimental R_{sh} data. $(E_{dis} - E_i)$, U_s and R_{dis} are taken as the fitting parameters. It was established that the good agreement of the experimental data with the fitting curves has been observed (see Figure 10) for values $(E_{dis} - E_i) = (0.34 \pm 0.02)$ eV and $U_s = (5 \pm 4) \times 10^{-8}$ eV, which were independent of USL. The obtained value $(E_{dis} - E_i)$ corresponds to the carrier activation energy $E_a \simeq 0.5E_g - (E_{dis} - E_i) \simeq 0.22$ eV, which is comparable to the values reported by other researcher. Thus activation energies $0.22 \div 0.25$ eV [57], 0.28 eV [58], 0.19 eV [59] and 0.23 eV [60] are associated with an impurity at the dislocation or with an intrinsic dislocstion levels.

The R_{dis} value decreases in the T–USL case and its relative changes ε_{Rdis} are shown in Table 1. On our opinion this is caused by an augmentation of A_{dis} in Eq. (17). The dislocation core atom displacement is parallel and normal to the current direction in the L–USL case and T–USL case respectively. As the result, in the T–USL case carriers are captured by dislocation levels from enlarged volume. It induces the effective surface area increase and the shunt resistance decrease.

3.5. Ultrasound influence on SSC conversion parameters

Figure 11 depicts an acoustically driven degradation of photocurrent, open–circuit voltage and the fill factor. The relative changes of these parameters are listed in the Table 1.

In the case of used illumination wavelength of $\lambda = 900$ nm, the photocurrent defined

by the electron-hole pair generation in the p–region mainly. If the base is several minority carrier diffusion lengths $L_n = \sqrt{\mu_n kT\tau_n/q}$, the J_{ph} can be written as [26, 61]

$$J_{ph} = \frac{W_{ph}(1-M)q\beta\lambda}{hc}\frac{\alpha L_n}{1+\alpha L_n}, \tag{18}$$

where α is the absorption coefficient, M is the reflection coefficient, β is the coefficient of quantum yield. Thereby J_{ph} strongly depends on τ_n. On the other hand, the minority carrier lifetime can be estimated from a photocurrent temperature dependence. We tool α temperature dependence from [26] (p.39, Eq. (18)), and supposed, that β and M were temperature independent, $L_n \sim T^{0.5}$. The last dependence was obtained from Figure 6. Then Eq. (18) was used by taking L_n as fitting parameter to fit the experimental temperature dependence of J_{ph}. The fitting results are shown on Figure 11(a) by curves.

The L_n values, which are obtained from a recombination current in the quasi-neutral region (106 ± 10 μm and 88 ± 10 μm for SC–R4 and SC–R15 respectively at 320 K without USL) and from a photocurrent temperature dependence (125 ± 15 μm and 99 ± 15 μm for SC–R4 and SC–R15), are comparable. The relative changes of lifetime, obtained from J_{ph}, $\varepsilon_{\tau n}^{Jph}$ are listed in the Table 1. The values of $\varepsilon_{\tau n}^{Jph}$ and $\varepsilon_{\tau n}$ agree qualitatively. The slight quantitative difference, which is observed in the T–USL case, can be deals with the AI change of L_n temperature dependence probably. Thus the ultrasound influence on photocurrent (and short-circuit current) is due to AI change of minority carrier lifetime, which is discussed above.

Unfortunately the analytical expressions for V_{oc} and FF are absent in the double–diode model case. To show V_{oc} and FF dependencies on τ_n, n, τ_g, and R_{sh} we have simulated I–V characteristics at different parameters value by using Eqs. (1) and (18). The values, that are close to investigated SSCs parameters, are used for simulation. The results are shown on Figure 12 and Figure 13.

One can see on Figure 12(a) and Figure 13(a) that τ_g decrease should lead to a decrement of both V_{oc} and FF. At the same time the open–circuit voltage and the fill factor dependencies on τ_n are weak for the investigated SSC. Figure 12(b) and Figure 13(b) show that the n as well as R_{sh} influence on V_{oc} and FF depends substantially on shunt resistance value. Thus if $R_{sh} > 10^5$ Ω (SC–R15 case) then V_{oc} increases with an ideality factor increment and both V_{oc} and FF don't depend on shunt resistance value practically. Whereas if $R_{sh} \leq 10^4$ Ω (SC–R4 case) then the open–circuit voltage and the fill factor decrease with shunt resistance decrement, but FF only depends on n weakly.

Thereby the discussed above AI decrease of τ_g leads to degradation of open–circuit voltage and the fill factor in the USL case. This effect is enhanced by AI R_{sh} decrease in the SC–R4 and is recovered partially by AI n increase in the SC–R15.

4. Conclusion

The experimental investigation of ultrasound influence on the silicon solar cell has been carried out in the temperature range from 290 to 340 K. The investigation has revealed
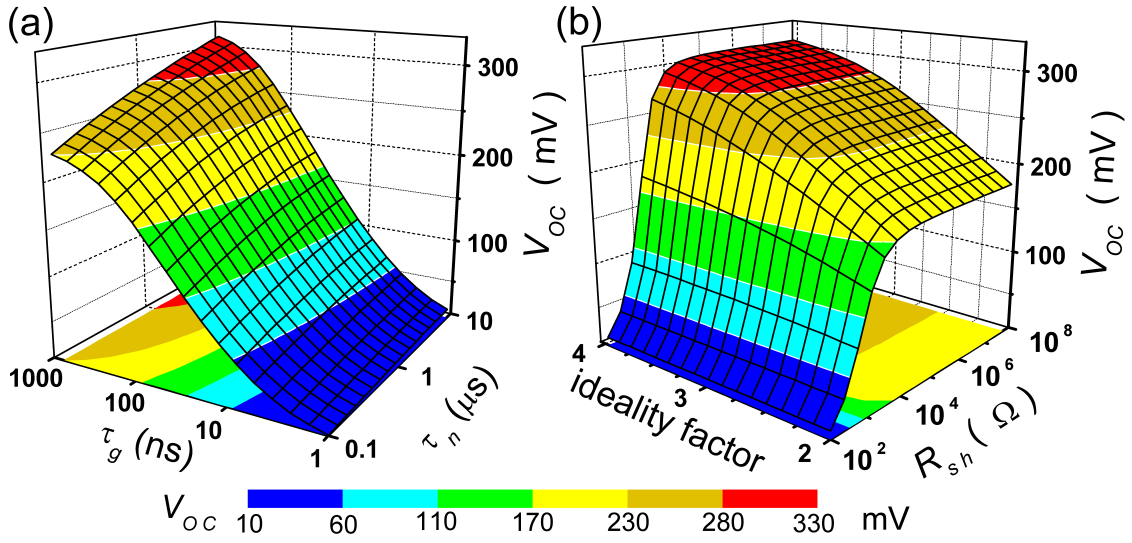
Figure 12. Simulated open–circuit voltage dependencies on SCR carrier lifetime and base carrier lifetime (a) and on ideality factor and shunt resistance (b). The constant values $n = 2.55$ (a), $R_{sh} = 5 \cdot 10^3$ Ω (a), $\tau_n = 3 \cdot 10^{-6}$ s (b), $\tau_g = 5 \cdot 10^{-8}$ s (b), and $T = 320$ K were used.
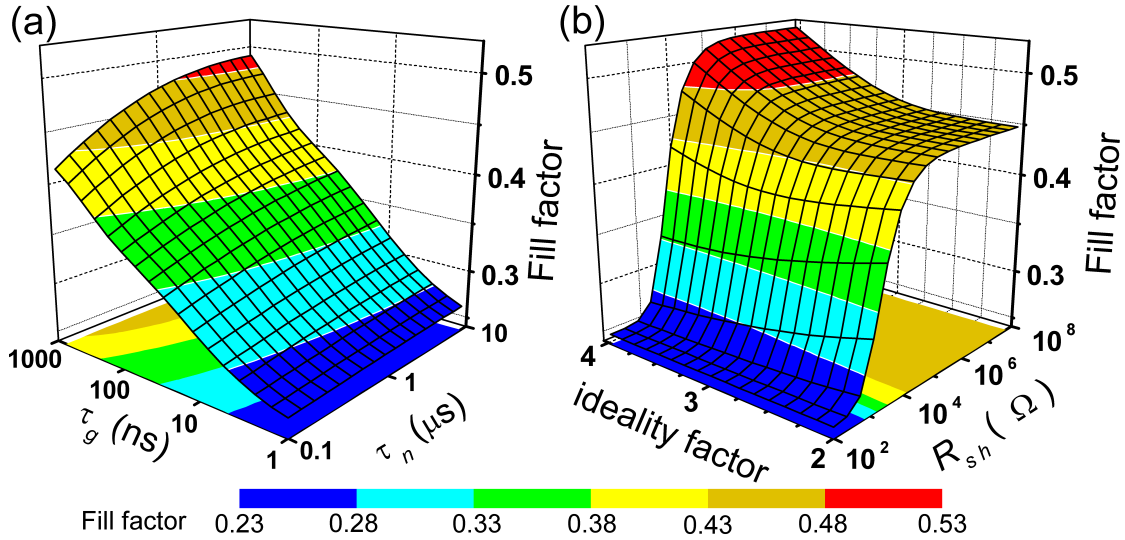

Figure 13. Simulated fill factor dependencies on SCR carrier lifetime and base carrier lifetime (a) and on ideality factor and shunt resistance (b). The constant values $n = 2.55$ (a), $R_{sh} = 5 \cdot 10^3$ Ω (a), $\tau_n = 3 \cdot 10^{-6}$ s (b), $\tau_g = 5 \cdot 10^{-8}$ s (b), and $T = 320$ K were used.

the acoustically driven reversible degradation of SSC parameters. It has been found out that the transverse ultrasound waves are more effective tools to affect silicon structure parameters than longitudinal ones. It has been given evidence that the degradation is due to the recombination amplification under the ultrasound wave action. The analysis has shown that the acoustically induced increase of carrier capture coefficient of point or extended defects is a reason of observed effects. The qualitative model of ultrasound influence, which is based on a change of a distance between defects or between components of defect complex under alternating deformation action, is proposed. It has been shown that the oxide precipitates are most likely defects, which take part in the acousto–defect interaction. Thus, ultrasound can be an effective tool for controlling silicon structure characteristics.

References

[1] Bothe K, Sinton R, Schmidt J. Fundamental boron–oxygen-related carrier lifetime limit in mono- and multicrystalline silicon. *Progress in Photovoltaics: Research and Applications* **13**(4), 2005: 287–296. DOI:10.1002/pip.586.

[2] Schmidt J, Bothe K, Macdonald D, Adey J, Jones R, Palmer D. Electronically stimulated degradation of silicon solar cells. *Journal of Materials Research* **21**(1), 2006: 5–12. DOI: 10.1557/JMR.2006.0012.

[3] Lindroos J, Savin H. Review of light-induced degradation in crystalline silicon solar cells. *Sol Energy Mater Sol Cells* **147**, 2016: 115–126. DOI:http://dx.doi.org/10.1016/j.solmat.2015.11.047.

[4] Vahlman H, Haarahiltunen A, Kwapil W, Schon J, Inglese A, Savin H. Modeling of light-induced degradation due to Cu precipitation in p–type silicon. II. Comparison of simulations and experiments. *J Appl Phys* **121**(19), 2017: 195704. DOI:10.1063/1.4983455.

[5] Naumann V, Lausch D, Hahnel A, Bauer J, Breitenstein O, Graff A, Werner M, Swatek S, Grober S, Bagdahn J, Hagendorf C. Explanation of potential-induced degradation of the shunting type by Na decoration of stacking faults in Si solar cells. *Sol Energy Mater Sol Cells* **120**, 2014: 383–389. DOI:10.1016/j.solmat.2013.06.015.

[6] Hoffmann S, Koehl M. Effect of humidity and temperature on the potential-induced degradation. *Progress in Photovoltaics: Research and Applications* **22**(2), 2012: 173–179. DOI: 10.1002/pip.2238.

[7] Hara K, Ogawa K, Okabayashi Y, Matsuzaki H, Masuda A. Influence of surface structure of n–type single–crystalline Si solar cells on potential–induced deInfluence. *Sol Energy Mater Sol Cells* **166**, 2017: 132–139. DOI:10.1016/j.solmat.2017.03.018.

[8] Bhat S, Rao A, Krishnan S, Sanjeev G, Puthanveettil SE. A study on the variation of c-Si solar cell parameters under 8 MeV electron irradiation. *Sol Energy Mater Sol Cells* **120**, 2014: 191–196. DOI:10.1016/j.solmat.2013.08.043.

[9] Karazhanov SZ. Mechanism for the anomalous degradation of silicon space solar cells. *Applied Physics Letters* **76**(19), 2000: 2689–2691. DOI:10.1063/1.126445.

[10] Ostapenko S. Defect passivation using ultrasound treatment: fundamentals and application. *Applied Physics A: Materials Science & Processing* **69**(2), 1999: 225–232. DOI: 10.1007/s003390050994.

[11] Ostrovskii I, Korotchenkov O, Olikh O, Podolyan A, Chupryna R, Torres-Cisneros M. Acoustically driven optical phenomena in bulk and low-dimensional semiconductors. *J Opt A: Pure Appl Opt* **3**(4), 2001: S82–S86. DOI:10.1088/1464-4258/3/4/364.

[12] Olikh OY, Voytenko KV, Burbelo RM. Ultrasound influence on I–V–T characteristics of silicon Schottky barrier structure. *Journal of Applied Physics* **117**(4), 2015: 044505. DOI: 10.1063/1.4906844.

[13] Olikh O. Features of dynamic acoustically induced modification of photovoltaic parameters of silicon solar cells. *Semiconductors* **45**(6), 2011: 798–804. DOI:10.1134/S1063782611060170.

[14] Davletova A, Karazhanov SZ. A study of electrical properties of dislocation engineered Si processed by ultrasound. *Journal of Physics and Chemistry of Solids* **70**(6), 2009: 989–992. DOI: 10.1016/j.jpcs.2009.05.009.

[15] Davletova A, Karazhanov SZ. Open-circuit voltage decay transient in dislocation-engineered Si p-n junction. *Journal of Physics D: Applied Physics* **41**(16), 2008: 165107. DOI:10.1088/0022-3727/41/16/165107.

[16] Melnik V, Olikh Y, Popov V, Romanyuk B, Goltvyanskii Y, Evtukh A. Characteristics of silicon p–n junction formed by ion implantation with in situ ultrasound treatment. *Materials Science & Engineering, B: Solid-State Materials for Advanced Technology* **124–125**, 2005: 327–330. DOI:10.1016/j.mseb.2005.08.039.

[17] Olikh O. Reversible influence of ultrasound on $\gamma-$irradiated Mo/n-Si Schottky barrier structure. *Ultrasonics* **56**, 2015: 545–550. DOI:10.1016/j.ultras.2014.10.008.

[18] Korotchenkov O, Grimmliss H. Long-wavelength acoustic-mode-enhanced electron emission from Se and Te donors in silicon. *Physical Review B* **52**(20), 1995: 14598–14606. DOI: 10.1103/PhysRevB.52.14598.

[19] Ostapenko SS, Bell RE. Ultrasound stimulated dissociation of Fe–B pairs in silicon. *Journal of Applied Physics* **77**(10), 1995: 5458–5460. DOI:10.1063/1.359243.

[20] Olikh OY. The Variation in Activity of Recombination Centers in Silicon pn Structures under the Conditions of Acoustic Loading. *Semiconductors* **43**(6), 2009: 745–750. DOI: 10.1134/S1063782609060116.

[21] Kropman D, Seeman V, Dolgov S, Medvids A. Effect of ultrasonic treatment on the defect structure of the Si–SiO$_2$ system. *Phys Status Solidi C* **13**(10–12), 2016: 793–797. DOI: 10.1002/pssc.201600052.

[22] Zaveryukhina N, Zaveryukhina E, Vlasov S, Zaveryukhin B. Acoustostimulated changes in the density of surface states and their energy spectrum in p–type silicon single crystals. *Technical Physics Letters* **34**(3), 2008: 241–243. DOI:10.1134/S106378500803019X.

[23] Mirsagatov SA, Sapaeva IB, Nazarov Z. Ultrasonic Annealing of Surface States in the Heterojunction of a p–Si/n–CdS/n^+–CdS Injection Photodiode. *Inorganic Materials* **51**(1), 2015: 1–4. DOI:10.1134/S0020168515010148.

[24] Sproul AB, Green MA. Intrinsic carrier concentration and minority-carrier mobility of silicon from 77 to 300 K. *J Appl Phys* **73**(3), 1993: 1214–1225. DOI:10.1063/1.353288.

[25] Schroder DK. *Semiconductor Material and Device Characterization.* New Jersey: John Wiley & Sons, third edition, 2006.

[26] McEvoy A, Markvart T, Castaner L, editors. *Solar Cells. Materials, Manufacture and Operation.* Oxford: Academic Press, second edition, 2013.

[27] Wang K, Ye M. Parameter determination of Schottky–barrier diode model using differential evolution. *Solid-State Electron* **53**(2), 2009: 234–240. DOI:10.1016/j.sse.2008.11.010.

[28] Olikh O, Voytenko K. On the mechanism of ultrasonic loading effect in silicon–based Schottky diodes. *Ultrasonics* **66**(1), 2016: 1–3. DOI:10.1016/j.ultras.2015.12.001.

[29] van der Heide ASH, Schonecker A, Bultman JH, Sinke WC. Explanation of High Solar Cell Diode Factors by Nonuniform Contact Resistance. *Progress in Photovoltaics: Research and Applications* **13**(1), 2005: 3–16. DOI:10.1002/pip.556.

[30] Beier J, Voss B. Humps in dark I-V-curves — Analysis and explanation. In *Proceedings of the 23rd IEEE Photovoltaic Specialists Conference.* 1993, 321–326. Louisville, KY, USA.

[31] Shah JM, Li YL, Gessmann T, Schubert EF. Experimental analysis and theoretical model for anomalously high ideality factors ($n \gg 2.0$) in AlGaN/GaN p–n junction diodes. *J Appl Phys* **94**(4), 2003: 2627–2630. DOI:10.1063/1.1593218.

[32] Kaminski A, Marchand JJ, Omari HE, Laugier A, Le QN, Sarti D. Conduction processes in silicon solar cells. In *Proceedings of the 1996 25th IEEE Photovoltaic Specialists Conference.*

1996, 573–576. Washington, DC, USA.

[33] Schenka A, Krumbein U. Coupled defect-level recombination: Theory and application to anomalous diode characteristics. *Journal of Applied Physics* **78**(5), 1995: 3185–3192. DOI: 10.1063/1.360007.

[34] Steingrube S, Breitenstein O, Ramspeck K, Glunz S, Schenk A, Altermatt PP. Explanation of commonly observed shunt currents in c-Si solar cells by means of recombination statistics beyond the Shockley-Read-Hall approximation. *Journal of Applied Physics* **110**(1), 2011: 014515. DOI: 10.1063/1.3607310.

[35] Breitenstein O, Bauer J, Altermatt PP, Ramspeck K. Influence of Defects on Solar Cell Characteristics. *Solid State Phenomena* **156–158**, 2010: 1–10. DOI:10.4028/www.scientific.net/SSP.156-158.1.

[36] Fahrenbruch A, Bube R. *Fundamentals of Solar Cells: Photovoltaic Solar Energy Conversion.* Academic Press, 1983.

[37] Sachenko A, Kostylyov V, Korkishko R, Kulish M, Sokolovskyi I, Vlasiuk V, Khomenko D. Peculiarities of the temperature dependences of silicon solar cells illuminated with light simulator. *Semiconductor Physics, Quantum Electronics & Optoelectronics* **18**(3), 2015: 259–266. DOI:10.15407/spqeo18.03.259.

[38] Mirzade F. Elastic wave propagation in a solid layer with laser-induced point defects. *J Appl Phys* **110**(6), 2011: 064906. DOI:10.1063/1.3633524.

[39] Peleshchak R, Kuzyk O, Dan'kiv O. Formation of Periodic Structures under the Influence of an Acousti Wave in Semiconductors with a Two-Component Defect Subsystem. *Ukr J Phys* **61**(8), 2016: 741–746. DOI:10.15407/ujpe61.08.0741.

[40] Thomas DG, Hopfield J, Augistyniak WM. Kinetics of Radiative Recombination at Randomly Distributed Donors and Acceptors. *Phys Rev* **140**(1A), 1965: A202–A220. DOI: 10.1103/PhysRev.140.A202.

[41] Murphy JD, Bothe K, Olmo M, Voronkov VV, Falster RJ. The effect of oxide precipitates on minority carrier lifetime in p–type silicon. *J Appl Phys* **110**(5), 2011: 053713. DOI: 10.1063/1.3632067.

[42] Kim M, Abbott M, Nampalli N, Wenham S, Stefani B, Hallam B. Modulating the extent of fast and slow boron-oxygen related degradation in Czochralski silicon by thermal annealing: Evidence of a single defect. *J Appl Phys* **121**(5), 2017: 053106. DOI:10.1063/1.4975685.

[43] Vahanissi V, Haarahiltunen A, Talvitie H, Yli-Koski M, Savin H. Impact of phosphorus gettering parameters and initial iron level on silicon solar cell properties. *Progress in Photovoltaics: Research and Applications* **21**(5), 2012: 1127–1135. DOI:10.1002/pip.2215.

[44] Schmidt J. Effect of Dissociation of Iron–Boron Pairs in Crystalline Silicon on Solar Cell Properties. *Progress in Photovoltaics: Research and Applications* **13**(4), 2005: 325–331. DOI: 10.1002/pip.594.

[45] Mchedlidze T, Weber J. Iron–related carrier traps near the n^+p–junctions of crystalline silicon solar cells: impacts of feedstock and of the fabrication processes. *Phys Status Solidi B* **251**(8), 2014: 1608–1613. DOI:10.1002/pssb.201451021.

[46] Mchedlidze T, Scheffler L, Weber J, Herms M, Neusel J, Osinniy V, Moller C, Lauer K. Local detection of deep carrier traps in the pn-junction of silicon solar cells. *J Appl Phys* **103**(01), 2013: 013901. DOI:10.1063/1.4807142.

[47] Murphy J, McGuire J, Bothe K, Voronkov V, Falster R. Minority carrier lifetime in silicon photovoltaics: The effect of oxygen precipitation. *Sol Energy Mater Sol Cells* **120**, 2014: 402–411. DOI:10.1016/j.solmat.2013.06.018.

[48] Schon J, Youssef A, Park S, Mundt LE, Niewelt T, Mack S, Nakajima K, Morishita K, Murai R, Jensen MA, Buonassisi T, Schubert MC. Identification of lifetime limiting defects by temperature– and injection-dependent photoluminescence imaging. *J Appl Phys* **120**(10), 2016: 105703. DOI:10.1063/1.4961465.

[49] Murphy JD, Bothe K, Krain R, Voronkov VV, Falster RJ. Parameterisation of injection-

dependent lifetime measurements in semiconductors in terms of Shockley–Read–Hall statistics: An application to oxide precipitates in silicon. *J Appl Phys* **111**(11), 2012: 113709. DOI: 10.1063/1.4725475.

[50] Chen L, Yu X, Chen P, Wang P, Gu X, Lu J, Yang D. Effect of oxygen precipitation on the performance of Czochralski silicon solar cells. *Sol Energy Mater Sol Cells* **95**(11), 2011: 3148–3151. DOI:10.1016/j.solmat.2011.06.044.

[51] Breitenstein O, Rakotoniaina JP, Al Rifai MH, Werner M. Shunt Types in Crystalline Silicon Solar Cells. *Progress in Photovoltaics: Research and Applications* **12**(7), 2004: 529–538. DOI: 10.1002/pip.544.

[52] Gopal V. A new approach to investigate leakage current mechanisms in infrared photodiodes from illuminated current-voltage characteristics. *J Appl Phys* **116**(8), 2014: 084502. DOI: 10.1063/1.4893899.

[53] Baker I, Maxey C. Summary of HgCdTe 2D Array Technology in the U.K. *J Electron Mater* **30**(6), 2001: 682–689. DOI:10.1007/BF02665856.

[54] Gopal V, Gupta S. Effect of Dislocations on the Zero-Bias Resistance-Area Product, Quantum Efficiency, and Spectral Response of LWIR HgCdTe Photovoltaic Detectors. *IEEE Trans Electron Devices* **50**(5), 2003: 1220–1226. DOI:10.1109/TED.2003.813230.

[55] Gopal V, Gupta S. Contribution of Dislocations to the Zero-Bias Resistance-Area Product of LWIR HgCdTe Photodiodes at Low Temperatures. *IEEE Trans Electron Devices* **51**(7), 2004: 1078–1083. DOI:10.1109/TED.2004.829857.

[56] Barth N, Jovanovic R, Ahzi S, Khaleel MA. PV panel single and double diode models: Optimization of the parameters and temperature dependence. *Sol Energy Mater Sol Cells* **148**, 2016: 87–98. DOI:10.1016/j.solmat.2015.09.003.

[57] Evans-Freeman J, Emiroglu D, Vernon-Parry K, Murphy J, Wilshaw PR. High resolution deep level transient spectroscopy applied to extended defects in silicon. *J Phys: Condens Matter* **17**(22), 2005: S2219–S2227. DOI:10.1088/0953-8984/17/22/009.

[58] Castaldini A, Cavalcoli D, Cavallini A, Pizzini S. Experimental Evidence of Dislocation Related Shallow States in p-Type Si. *Phys Rev Lett* **95**(7), 2005: 076401. DOI: 10.1103/PhysRevLett.95.076401.

[59] Omling P, Weber ER, Montelius L, Alexander H, Michel J. Electrical properties of dislocations and point defects in plastically deformed silicon. *Phys Rev B* **32**(10), 1985: 6571–6581. DOI: 10.1103/PhysRevB.32.6571.

[60] Ogawa M, Kamiya S, Izumi H, Tokuda Y. Electronic properties of dislocations introduced mechanically at room temperature on a single crystal silicon surface. *Physica B: Physics of Condensed Matter* **407**(15), 2012: 3034–3037. DOI:doi:10.1016/j.physb.2011.09.139.

[61] Razeghi M, Rogalski A. Semiconductor ultraviolet detectors. *Journal of Applied Physics* **79**(10), 1996: 7433–7473. DOI:10.1063/1.362677.